




Article

An Assessment of Persistent Acoustic Monitoring of a Nuclear Reactor during Full Power Generation

Edna S. Cárdenas ^{1,*}, Samuel K. Takazawa ², Milton A. Garcés ², David L. Chichester ¹, Riley D. Hunley ^{3,4} and Chris D. Young ³

¹ Idaho National Laboratory, Idaho Falls, ID 83415, USA

² Infrasound Laboratory, Hawaii Institute of Geophysics and Planetology, School of Ocean and Earth Science and Technology, University of Hawai'i, Manoa, HI 96740, USA

³ Oak Ridge National Laboratory, Oak Ridge, TN 37830, USA

⁴ TRISO-X, LLC, Oak Ridge, TN 37830, USA

* Correspondence: edna.cardenas@inl.gov

Abstract: Persistent low-frequency (<180 Hz) acoustic detection took place within the boundaries of Oak Ridge National Laboratory to monitor full power operations of the High Flux Isotope Reactor. Three acoustic sensors were installed at distances of 69, 101, and 914 m from the northeast corner of the cooling towers to monitor and assess four reactor power generation cycles. Features were extracted from power spectral density calculations where data were collected during reactor on and off operations. Diverse spectral features were present during full reactor power, including a 21.4 Hz fundamental frequency and ascending harmonics. Using bandpass filters, these related frequencies were isolated and summed, and the root mean square energy was calculated. The method of isolating and summing characteristic features provided a significant improvement in identifying acoustic behavior related to reactor power when the raw signals were obscured by noise.

Keywords: nuclear reactor; persistent monitoring; cooling tower fans



Citation: Cárdenas, E.S.; Takazawa, S.K.; Garcés, M.A.; Chichester, D.L.; Hunley, R.D.; Young, C.D. An Assessment of Persistent Acoustic Monitoring of a Nuclear Reactor during Full Power Generation. *Acoustics* **2023**, *5*, 429–443. <https://doi.org/10.3390/acoustics5020025>

Academic Editors: Andrew Y.

T. Leung and Jian Kang

Received: 15 December 2022

Revised: 13 March 2023

Accepted: 10 April 2023

Published: 28 April 2023



Copyright: © 2023 by the authors. Licensee MDPI, Basel, Switzerland. This article is an open access article distributed under the terms and conditions of the Creative Commons Attribution (CC BY) license (<https://creativecommons.org/licenses/by/4.0/>).

1. Introduction

Infrasound and low-frequency acoustic monitoring has been widely used to inform and alert researchers of potentially devastating natural phenomena such as volcanos, typhoons, and earthquakes [1–9]. While research focused on remote acoustic monitoring began with natural events, the field since has progressed into monitoring anthropogenic sources [10,11]. Methods of detecting anthropogenic sources that are matters of public concern or interest, such as chemical and nuclear explosions, missile and rocket launches, and spacecraft re-entries, were developed and continue to be investigated [12–17]. The detection of more pervasive sources, such as the movement of bridges and the operation of wind turbines, has also been studied [18–20]. Infrasound and low-frequency acoustic studies continue to explore emissions from industrial and mechanical sources including vehicles, agricultural machinery, and hydraulic systems [21–25]. Nuclear facilities present a relatively new venue for infrasound and low-frequency acoustic research and monitoring [26–29].

The implementation of monitoring techniques at nuclear facilities has been an ongoing topic of research in areas concerned with diagnostic evaluations and safeguards. Recent research, performed under the Multi-Informatics for Nuclear Operating Scenarios (MINOS) venture, have reported infrasound and low-frequency acoustic detection during power generation of the High Flux Isotope Reactor (HFIR) facility at Oak Ridge National Laboratory (ORNL) [30–33]. The ORNL campus serves as a testbed for multi-sensor deployment and data fusion research. The HFIR is cooled during operation by a primary and secondary cooling system. Heat from the primary cooling system is transferred to the secondary cooling system and finally dissipated into the atmosphere. The secondary system controls heat dissipation through circulating fans attached to the heat transfer exit

of four cooling fans [34,35]. Studies have shown that large fans and cooling towers generate infrasound and low-frequency acoustics [35–37]. Monitoring for acoustic signals at nuclear reactor facilities could therefore be used for diagnostic applications both when the source is accessible and when it is inaccessible due to high radiation fields or other obstructions.

The objective of this paper is to complement reported studies, performed under the MINOS venture, that describe acoustic monitoring techniques made during the operation of the HFIR. A key aspect of this work is to explore acoustic monitoring in nonideal conditions, including the absence of local meteorological data. In the paper by Marcillo et al., the authors reported on seismoacoustic monitoring from a single sensing station during a single HFIR operating cycle that included start-up, steady-state, and shutdown [30]. The authors observed a frequency measured at approximately 21.4 Hz and related harmonics from both the seismic and acoustic sensing channels that they postulated are related to the cooling tower fans. The tonal frequencies reported were present during full reactor power and were absent when the reactor was not operating. They report that the 21.4 Hz fundamental frequency drops to 18 Hz in coincidence with air temperature variances that result in operational changes in the cooling tower fans.

Rao et al. predicted HFIR power levels using data fusion, where a detailed description of the use of pumps and fans for controlling coolant flow and heat dissipation in the reactor's primary and secondary cooling systems was given [35]. The paper also presents the use of multiple sensing modalities, including acoustic sensors, for monitoring these systems. To test their data fusion methods, a single reactor start-up cycle was operated under a directed data collection campaign. The reactor power was increased in discrete steps similarly to typical start-up operations; however, the power was held at those steps for longer than is generally maintained. The results showed increased predictive certainty with the inclusion of an increasing number of sensing modalities, including acoustic sensors. The authors showed that the acoustic activity from the aggregate operation of four cooling fans increases in steps as reactor power increases, although with varying degrees of acoustic activity at each reactor power level.

Eaton et al. described an algorithm developed to successfully predict the rotational speeds of cooling tower fan rotors using acoustic signals collected at the Advanced Test Reactor (ATR) at Idaho National Laboratory and the HFIR at ORNL [33]. The acoustic signals measured at the ATR were collected using Samsung Galaxy 8 smartphones in the same way as those collected for the analysis in this paper. The acoustic signals measured at the HFIR were collected by infrasound sensors identical to those described in the paper by Marcillo et al. Data from separate four-hour time windows were collected from the installed sensors at the ATR and HFIR for analysis. The authors detail design and operational characteristics of two dual-speed and two variable-speed cooling tower fans at the HFIR and present acoustic signals generated during fan operation, which include a tone present at approximately 21.4 Hz for dual-speed fans that is identical to that described by Marcillo et al. The paper further identifies other frequencies that are present from the operation of variable-speed fans, as well as the calculation of blades speeds and specifications.

The present paper describes the measurement of infrasound and low-frequency acoustic signals from three sensors located near the HFIR and within the boundaries of ORNL. An assessment of measurements collected during four reactor operating cycles was performed. The acoustic sensors reported here differ from those utilized by Marcillo et al. and Rao et al., but they did detect identical tonal frequencies to those reported by Marcillo et al. and Eaton et al. This paper increases the depth of information regarding infrasound and low-frequency acoustic monitoring of the HFIR by including signals from additional reactor operating cycles and acoustic sensors located at varying distances from the reactor. This paper also describes a method for determining dominant energy peaks and results from implementing the same method on collected signals. The results show consistency in frequency from the dominant acoustic signals between reactor cycles when operating at full power, albeit with small frequency fluctuations. The fusion methods utilized by Rao et al. did not include varying sensor distances, nor did those reported by Marcillo et al.

or Eaton et al. Results from this paper show acoustic detection related to reactor power at distances beyond those previously reported. This paper describes an analysis method that exposes acoustic signals, obscured by noise, that were generated from the HFIR under full power operations. The work herein intends to provide insight into acoustic monitoring techniques and methods useful for determining reactor power operations at ORNL.

2. Materials and Methods

Data collected for this work were obtained under the MINOS venture and include infrasound and low-frequency (<180 Hz) acoustic signals that were detected using the RedVox Infrasound Recorder software application for Android, as well as the built-in microphone included on Samsung Galaxy 10 smartphones [38]. Samples were collected at a rate of 800 Hz with the smartphones operating persistently, with only short and infrequent dropouts in data collection during the MINOS venture and throughout HFIR operations from November 2018 to October 2021. Multiple smartphones were deployed during this data collection campaign, and this work focuses on three of them. Their identifying numbers (IDs), the distance from the northeast corner of the HFIR cooling towers (LAT = 35.91755, LONG = -84.30215), the distance from the approximate center of the high bay at the HFIR facility (LAT = 35.917640, LONG = -84.303346), and location descriptions are listed in Table 1. All smartphones were deployed within ORNL boundaries. Figures 1 and 2 show the phone locations relative to the HFIR cooling tower. The phones used in this research were located outdoors and installed inside weatherized enclosures with vents to allow for air flow and temperature regulation. Phone 33 was in its enclosure attached to a utility pole that sat on a bluff overlooking the HFIR cooling tower. Phone 35 (also in its enclosure) was around the corner from the HFIR truck lock door. The line of sight between Phone 35 and the HFIR cooling tower was obstructed by the truck lock door and other structures, as observed in Figure 1. Phone 40 was located in its enclosure near a communications tower on a ridge overlooking the HFIR cooling tower, shown in Figure 2.

Data were streamed from the phones in real time to RedVox cloud servers and downloaded for later analysis [38]. This study included data collected during HFIR operating cycles 487, 488-B, 489, and 490. For each cycle, analysis included start-up operations and data measured during steady-state reactor power immediately following start-up. The analysis also included data measured during steady-state reactor power immediately prior to and including shutdown. The times associated with each HFIR operating cycle are displayed in Coordinated Universal Time (UTC) in Table 2.

Table 1. Smartphone locations.

Smartphone ID	Approx. Distance from Cooling Towers, HFIR Facility	Location Description
Phone 33	69 m, 100 m	1 m above ground on bluff overlooking HFIR cooling towers
Phone 35	101 m, 34 m	1 m above ground near truck airlock door at HFIR building
Phone 40	914 m, 900 m	1.2 m above ground near communications tower on ridge overlooking HFIR

Table 2. Analysis times for the HFIR operating cycles presented.

HFIR Cycle and Operation	Start Time (UTC)	End Time (UTC)
487 start-up	28 April 2020 11:19:00	28 April 2020 14:19:00
487 shutdown	23 May 2020 15:02:00	23 May 2020 17:02:00
488-B start-up	12 June 2020 11:17:00	12 June 2020 14:17:00
488-B shutdown	7 July 2020 19:14:00	7 July 2020 21:14:00
489 start-up	18 August 2020 13:15:00	18 August 2020 15:35:00
489 shutdown	12 September 2020 21:32:00	12 September 2020 23:32:00
490 start-up	2 March 2021 18:16:00	2 March 2021 21:46:00
490 shutdown	27 March 2021 06:19:00	27 March 2021 08:19:00



Figure 1. Aerial map showing the locations of Phone 33 and Phone 35 in relation to the HFIR cooling tower. Google Earth $35^{\circ}55'05.30''$ N, $84^{\circ}18'10.97''$ W.



Figure 2. Aerial map showing Phone 40 in relation to the HFIR cooling tower. Google Earth $35^{\circ}54'53.11''$ N, $84^{\circ}18'09.98''$ W.

The analysis includes an examination of minimally processed raw waveforms to determine if any relevant features were visible. Processing consisted of de-trending followed by filtering of the waveforms with a second-order bandpass filter. The filter excluded frequencies lower and higher than 1 Hz and 180 Hz, respectively. The energy of the filtered signal was calculated by taking the root mean square (RMS) amplitude over 60 s with no overlap. The resulting RMS was then smoothed with a rolling median applied over 300 s to simulate the results of Marcillo et al. while keeping a higher time resolution. This second-order RMS was compared against related HFIR parametric data (i.e., reactor power estimates). Results from the raw RMS showed that measurements from Phone 33 generally behaved similarly to HFIR power; results were less successful for data measured from

Phone 35 and Phone 40, which were located farther away from the HFIR cooling towers and had obstructions between the phones and the cooling tower.

An additional analysis method was tested that was based on using the dominant frequencies active during reactor steady-state full power operation (FPO). To investigate key frequencies, spectral analysis was conducted by finding the power spectral density (PSD) of the filtered waveform by applying the Welch method with 20 s time windows and a 75% overlap [39]. To calculate the PSDs, data were collected at the start of HFIR FPO and for an additional 20 min. These data were background subtracted using data collected for 20 min just prior to reactor start-up. For shutdown operations, PSDs were calculated using data collected in the 20 min just prior to reactor shutdown during FPO. These FPO data were background subtracted using data collected for 20 min starting at the end-of-cycle outage. The PSD ratio highlights key frequencies that are unique to steady-state FPO.

The fundamental and related harmonic frequencies, determined from the PSD, were isolated by applying a second-order multi-bandpass filter with edges of 0.05 Hz on either side of the center of each frequency. A second RMS was calculated from 60 s time windows with no overlap followed by smoothing. Smoothing was performed with a rolling median applied over 300 s, which was identical to the method performed on the raw acoustic energy. This method of isolating characteristic frequencies with a narrow 1 Hz filter resulted in observed acoustic power that behaved similarly to the reactor power for all three phones.

3. Results and Discussion

Analysis and reported results use data collected at ORNL during four HFIR operating cycles. Ground truth (i.e., HFIR parametric power data) was obtained and is compared to recorded acoustic signals. During a typical HFIR cycle, the power is controlled at start-up and increases gradually in steps. Once the reactor reaches maximum power, it typically remains at a steady state until shutdown. At the end of each cycle, the reactor is shut down with power decreasing rapidly.

Results in this section use data collected from each smartphone for each reactor cycle at start-up and shutdown. The raw acoustic energy is determined by using a second-order bandpass filter that cuts out lower and upper frequencies, followed by calculation of the RMS. HFIR parametric power is overlaid against the raw acoustic energy for comparison. Additionally, the PSD was calculated to determine characteristic frequencies present during steady-state FPO. Finally, the RMS values for the approximate 21.4 Hz fundamental frequency and related harmonics are isolated using a second-order multi-bandpass filter and summed. This is referred to as the summed RMS power. The results are presented with HFIR parametric power overlaid for comparison.

3.1. HFIR Cycle 487

3.1.1. Cycle 487 Start-Up

Power generation from HFIR Cycle 487 was increased in discrete steps of 10%, 30%, 50%, 70%, 90%, and 100%, as documented in the reactor parametric data overlaid with the raw acoustic RMS power presented in Figure 3. The 10%, 30%, 50%, 70%, 90%, and 100% stepwise increase in reactor power was observed in all cycles presented here. The figure shows that the reactor increased in discrete steps, and although the raw acoustic RMS power increased, it was not generated in discrete steps. The raw acoustic RMS power presented from Phone 33 and Phone 35, as observed in Figure 3a,b, respectively, was lower in strength while the reactor is not operating and generally and gradually increased in strength as reactor power increased. Both phones show a dip in acoustic power when the reactor changed to 70% power. The raw acoustic RMS power then reached and maintained nearly constant maximum power as the reactor reached and maintained maximum power. Furthermore, while raw acoustic RMS power measured by Phone 40 increased as the reactor increased to 10% and 50% power, as shown in Figure 3c, acoustic behavior did not follow the generation of reactor power in the remainder of the time presented.

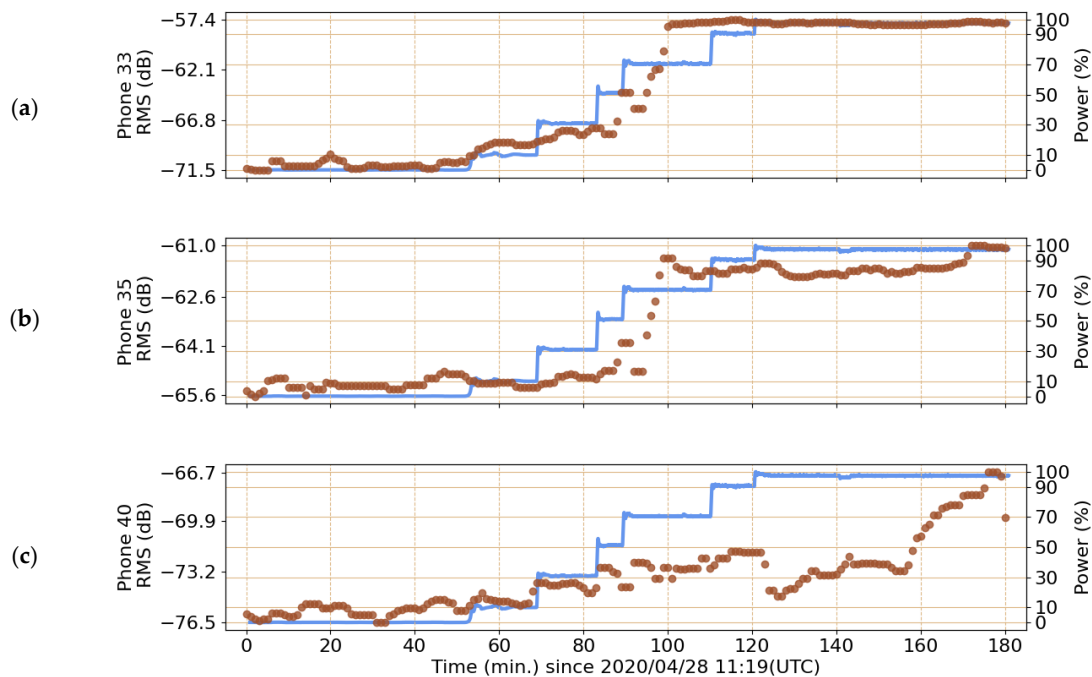


Figure 3. Raw acoustic RMS power (•) with parametric ground truth for HFIR Cycle 487 during start-up operations overlaid (–). Data collected from smartphones 33, 35, and 40 are shown in (a), (b), and (c), respectively.

To determine the acoustic features present during HFIR full power operations, calculation of the power density ratio (PDR) was performed. The ratio compares the data collected beginning 30 min immediately following the reactor reaching full power with the data collected in the 30 min immediately prior to the reactor beginning start-up operations. As shown in Figure 4, the PDR shows a 21.4 Hz fundamental frequency is present in all three phones, along with seven ascending harmonics. Each tone is observed in all three phones with varying levels of signal-to-noise (note that the lower frequencies can be seen more clearly in Section 3.4). All phones measure the same central fundamental frequency and harmonics when the reactor is operating at a steady state during the cycles examined; however, small variations in frequency occur (within 1.2%), as listed in Table 3. Frequency variations associated with the fundamental frequencies extend to the related harmonics, which are not shown. These variations may be due to thermal changes; however, further work is needed to explore those effects [40]. The central frequencies listed in Table 3 and related harmonics were used to calculate the summed RMS acoustic power presented in Figure 5, as well as in the related figures for each reactor power cycle presented here. Furthermore, as shown in Figure 4c, a low-frequency hump (below approximately 10.7 Hz) is present in Phone 40. Based on our understanding of this measurement campaign, this hump in the data is due to low-frequency noise that may be caused by wind.

Table 3. List of fundamental frequencies measured for HFIR cycle start-up and shutdown operations.

Cycle	Center of Fundamental Frequency (Hz)
487 start-up	21.40
487 shutdown	21.38
488-B start-up	21.18
488-B shutdown	21.40
489 start-up	21.40
489 shutdown	21.38
490 start-up	21.15
490 shutdown	21.14

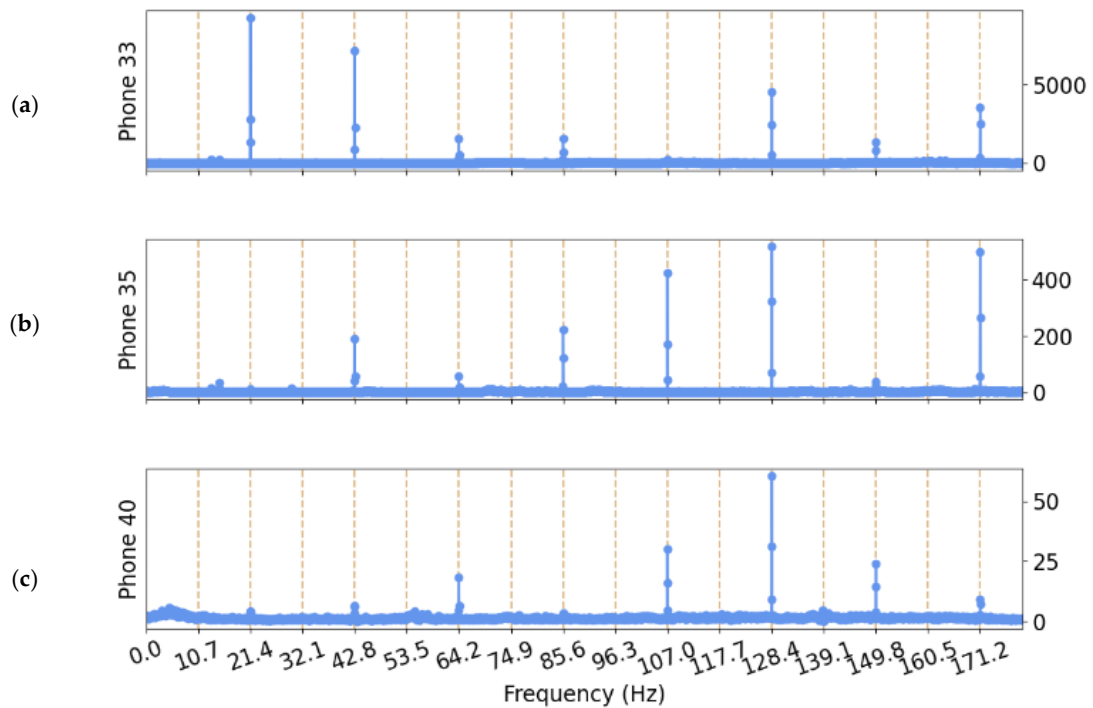


Figure 4. Power density ratios of HFIR Cycle 487 during start-up operations for smartphones 33, 35, and 40 are shown in (a), (b), and (c), respectively.

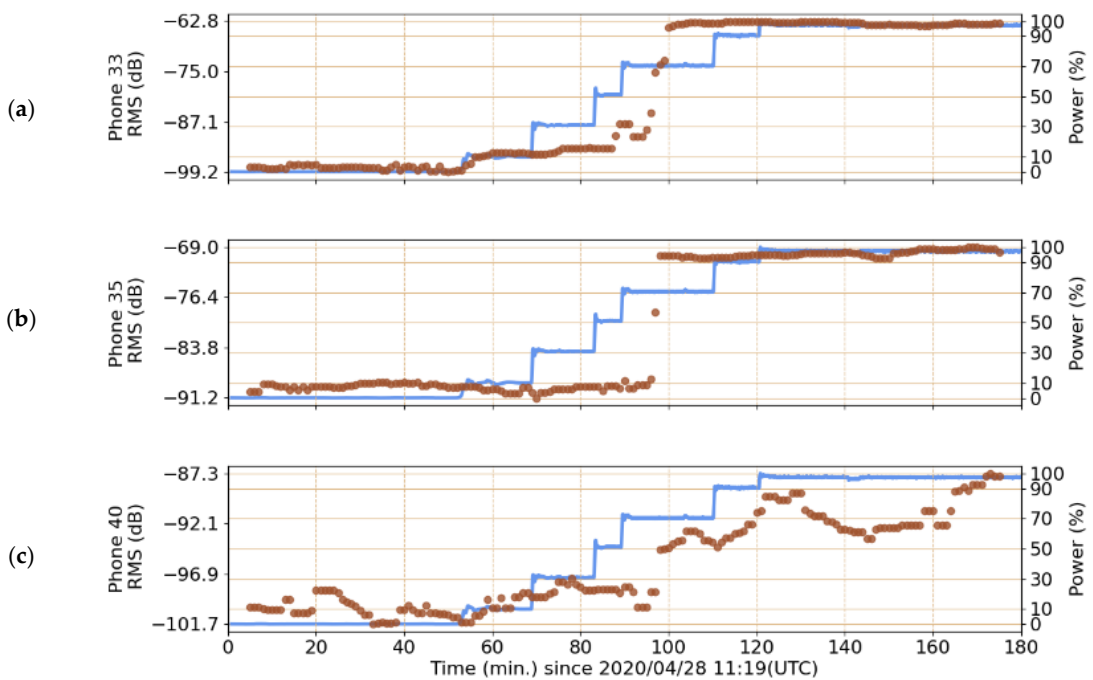


Figure 5. Summed RMS acoustic power (●) with parametric ground truth for HFIR Cycle 487 start-up overlaid (–). Data collected from smartphones 33, 35, and 40 are shown in (a), (b), and (c), respectively.

The summed bandpass-filtered RMS power, as presented in Figure 5, showed a significant improvement in following the behavior of the reactor in all three phones. Acoustic power increased in all three phones during the reactor start-up cycle. Phone 33 and Phone 35, as observed in Figure 5a,b, respectively, maintained relatively constant minimum and maximum power levels during reactor minimum and maximum power, respectively; however, during reactor start-up, Phone 33 recorded a 10% increase in decibel power as

the reactor reached 10% power. Phone 33 increased just prior to the reactor reaching 70% power and then dipped similarly to raw RMS acoustic power. The summed RMS acoustic power in Phone 35 dramatically increased from minimum to maximum during the time when the reactor maintained 70% power. Once the summed RMS acoustic power reached maximum power in Phone 35, it remained relatively steady in contrast to the behavior observed for raw RMS acoustic power. Furthermore, the summed RMS acoustic power collected from Phone 40, as presented in Figure 5c, increased as the reactor increased from 10% and 30%. Most prominently, the summed RMS acoustic power increased as the reactor reached 70%, as well as when it reached maximum power. These observations were not evident in the raw RMS acoustic power for Phone 40.

3.1.2. Cycle 487 Shutdown

In both the raw and summed RMS acoustic powers presented in Figure 6, the acoustic power measured by Phone 33 remained consistent and closely followed the behavior of reactor power, as shown in Figure 6a. The summed RMS acoustic behavior for Phone 35, observed in Figure 6b, followed a similar pattern to that observed with Phone 33. The raw RMS acoustic power for Phone 35 showed minor deviations from reactor power. In addition, noise obscures the acoustic signals relative to reactor power changes in the raw RMS power for Phone 40, as shown in Figure 6c. However, the noise is reduced by implementing the summed RMS acoustic power for Phone 40. Moreover, in all three phones, maximum acoustic power is maintained for approximately 10 min following reactor shutdown. This indicates cooling tower fan activity following reactor shutdown.

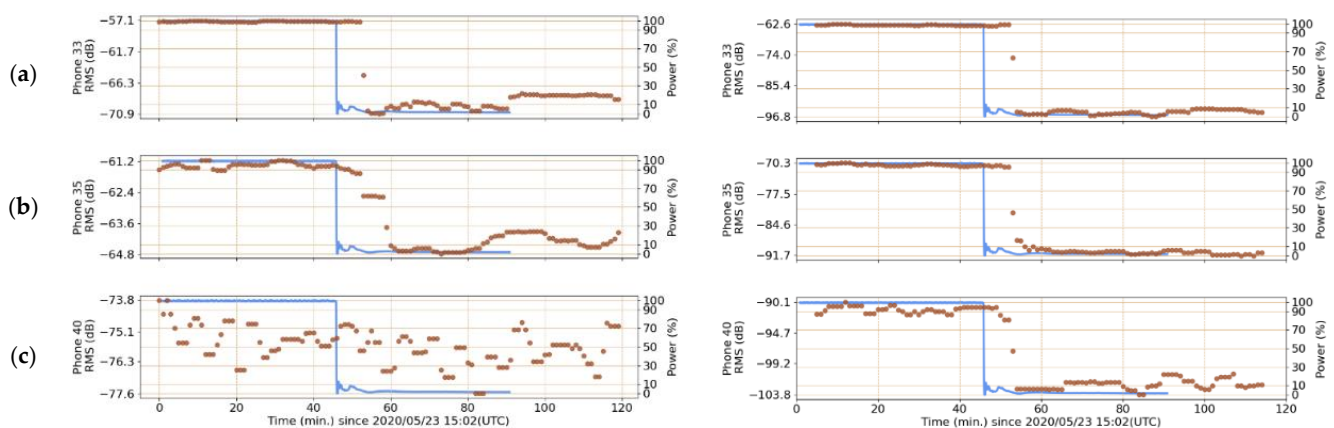


Figure 6. Acoustic RMS power (●) calculated from the raw waveform (left) and isolation and summing of the characteristic harmonics (right) for Phone 33, 35, and 40 are shown in (a), (b), and (c), respectively. The estimated reactor power for HFIR Cycle 487 shutdown (–) is overlaid for comparison.

3.2. HFIR Cycle 488-B

Cycle 488-B start-up analysis is provided in the Supplementary Materials.

Cycle 488-B Shutdown

Excluding an acoustic power maximum in Phone 33 that remained relatively constant during steady-state prior to shutdown, shown in Figure 7a, all three phones showed behavior that was seemingly unrelated to reactor power. In addition, a power increase began at approximately 85 min and was more defined in the summed RMS than the in the raw RMS acoustic power. This acoustic power maximum lasted for about 15 min and then abruptly decreased. Although the source of this acoustic power is not confirmed, issues with fan noise were recorded in the HFIR logs in the days leading up to the shutdown. Given the notes recorded in the HFIR logs and the claims made by Marcillo et al. and Eaton et al., the authors suspect the fans continued to operate following shutdown; however, this could not be verified.

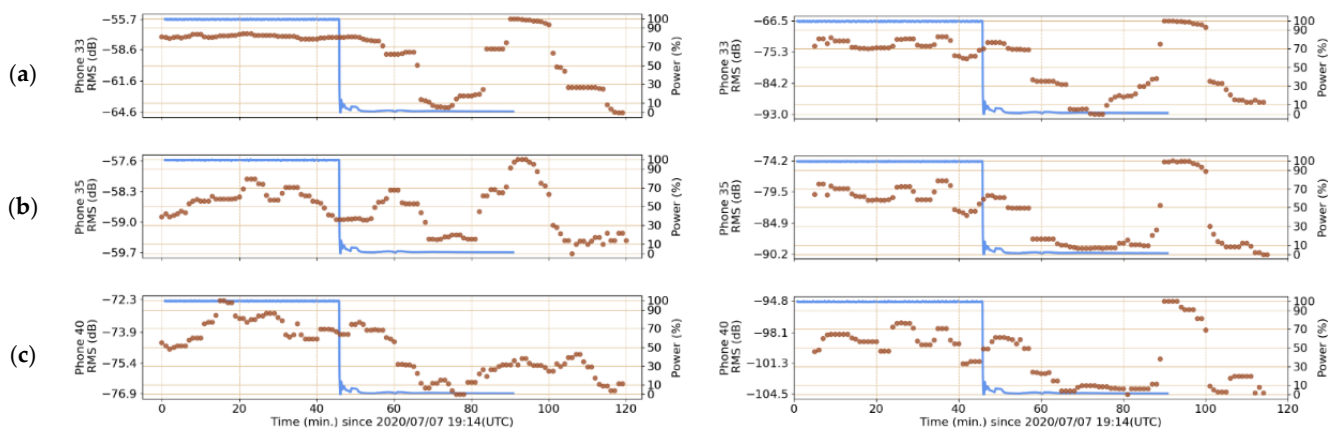


Figure 7. Acoustic RMS power (●) for HFIR Cycle 488-B shutdown calculated from the raw waveform (left) and isolation and summing of the characteristic harmonics (right) for Phone 33, 35, and 40 are shown in (a), (b), and (c), respectively. The estimated reactor power (–) is overlaid for comparison.

3.3. HFIR Cycle 489

Cycle 489 start-up analysis is provided in the Supplementary Materials.

Cycle 489 Shutdown

As with Cycle 487 and Cycle 488-B, the summed RMS acoustic power generated during Cycle 489 shutdown, shown in Figure 8, behaved more closely to reactor power than that observed in the raw RMS acoustic power. For all three phones, there was a nearly constant steady-state summed RMS acoustic power during reactor steady-state, which decreased immediately following reactor shutdown. Markedly and in contrast to reactor parametric data, the summed RMS acoustic power observed in data collected by all three phones has a clear dip during steady-state reactor power at approximately 21:38 UTC. At 21:40 UTC, the reactor operation logs reported that a cooling tower fan tripped and was reset. The nearness in time of the acoustic power dip and the logged event reaffirmed that the cooling tower fans were the dominant source of acoustic power generation during reactor operation. This assertion is further supported by the behavior of acoustic power following reactor shutdown. The summed RMS acoustic power dramatically increased to a maximum approximately 20 min following reactor shutdown. Although fan operations are not reported in the reactor operation logs following shutdown, it was recorded that the reactor operators planned to perform an investigation of fan issues following reactor shutdown. The acoustic data affirms the motivation for this investigation and indicates that the cooling tower fans resumed at approximately 22:36.

3.4. HFIR Cycle 490

Cycle 490 start-up analysis is provided in the Supplementary Materials.

Cycle 490 Shutdown

As with the previous cycles presented here, reactor power shut down abruptly, as observed in the parametric data presented in Figure 9. Both the raw and summed RMS acoustic power for Phone 33 and 35, shown in Figure 9a,b, respectively, behaved similarly, with the acoustic power maximum occurring at reactor FPO and the acoustic power minimum occurring at end-of-cycle power outage. For 9 min following reactor shutdown, the raw RMS acoustic power remained at a steady-state maximum, while the summed RMS acoustic power gradually decreased from maximum power.

In contrast to the raw RMS acoustic power calculated for Phone 40 and observed in Figure 9c, the summed RMS acoustic power behaved similarly to Phone 33 and 35. The difference in acoustic behavior between the raw and summed RMS power illustrated the benefits of isolating and summing the key frequencies determined in the PDR. In addition,

the increased acoustic activity in the 9 min following reactor shutdown, observed in the summed RMS acoustic power for all three phones, points to a generating source separate from, but correlated to, reactor power. This source is likely the operation of the HFIR cooling tower fans, as supported by the analysis in this paper for previous cycles and by the MINOS papers cited herein.

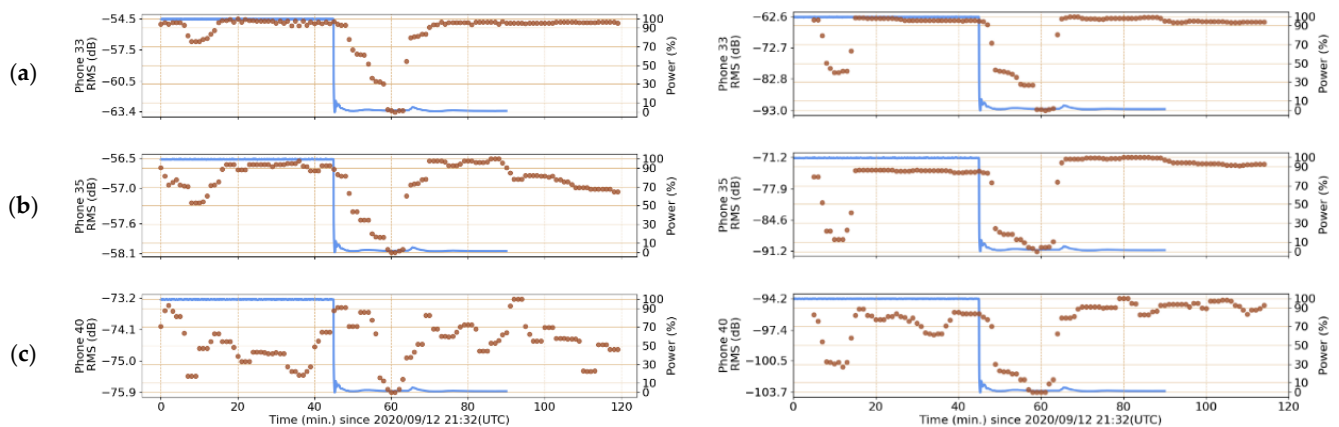


Figure 8. Acoustic RMS power (●) for HFIR Cycle 489 shutdown operations calculated from the raw waveform (left) and isolation and summing of the characteristic harmonics (right) for Phone 33, 35, and 40 are shown in (a), (b), and (c), respectively. The estimated reactor power (–) is overlaid for comparison.

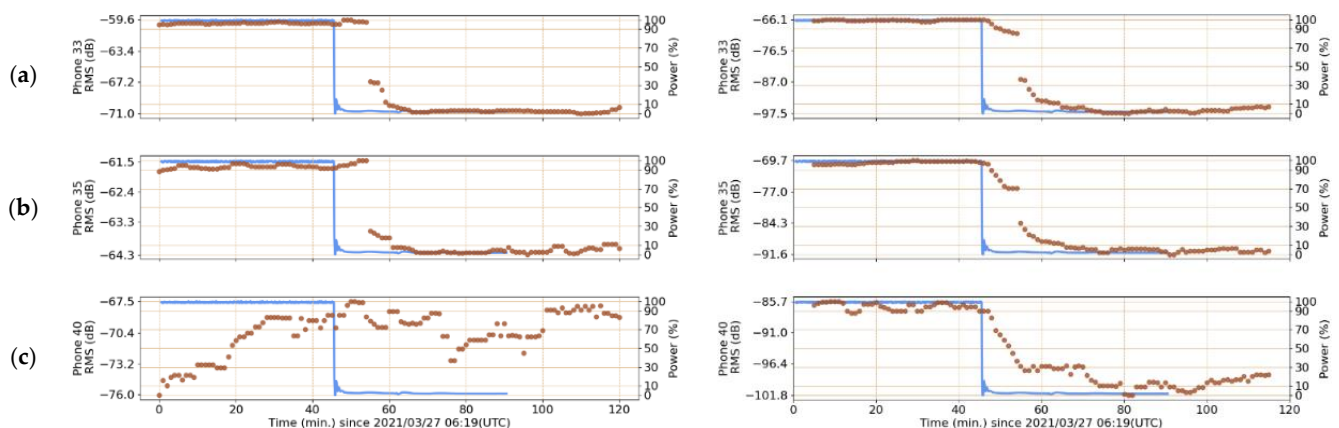


Figure 9. Acoustic RMS power (●) for HFIR Cycle 490 shutdown operations calculated from the raw waveform (left) and isolation and summing of the characteristic harmonics (right) for Phone 33, 35, and 40 are shown in (a), (b), and (c), respectively. The estimated reactor power (–) is overlaid for comparison.

3.5. Observation of Additional Frequencies Related to Fan Operations

The results presented in Section 3.3 focused on isolating the 21.4 Hz fundamental frequency and related harmonics that occur during HFIR full power operation. The paper by Eaton et al. discussed the relationship of additional acoustic signals related to operation of the dual-speed and variable-speed fans [33]. These additional acoustic signals were observed in this investigation and are discussed here for completeness. For brevity, this discussion will only include observations presented for HFIR Cycle 487; however, the signals were observed in all cycles discussed in Section 3.3.

In [33], the authors showed two time-averaged frequency spectra—one that showed all frequencies emitted during power generation, within the range of frequencies presented, and one where steady-state operations are background subtracted from the total. The total spectrum showed unchanging frequencies (e.g., those related to the cooling tower dual-

speed fans), while changing features (e.g., those related to variable-speed fans) remained in the background subtracted spectrum. The total spectrum included a peak at approximately 21.4 Hz. This frequency and its related harmonics were discussed in Section 3.3 and in the study by Marcillo et al. [30]. In addition to the 21.4 Hz fundamental frequency, features at 10.8 Hz and 15.0 Hz were identified by [33] as the dual-speed fan's blade passing and motor frequencies, respectively, when the 1800 RPM motor is operating at half speed. These additional peaks are clearly observed in this examination in the PDR calculated with data collected from Phone 33 and 35 and presented in Figure 10a,b, respectively. The peaks are likely obscured in Phone 40, as observed in Figure 10c, by low-frequency noise. In addition to the frequencies identified for the dual-speed fans [33], the authors mention but do not identify the maximum rotational speed of the HFIR cooling tower fans as 162 RPM. This rotational speed equates to 2.7 Hz and is visible in the PDRs for Phone 33 and 35.

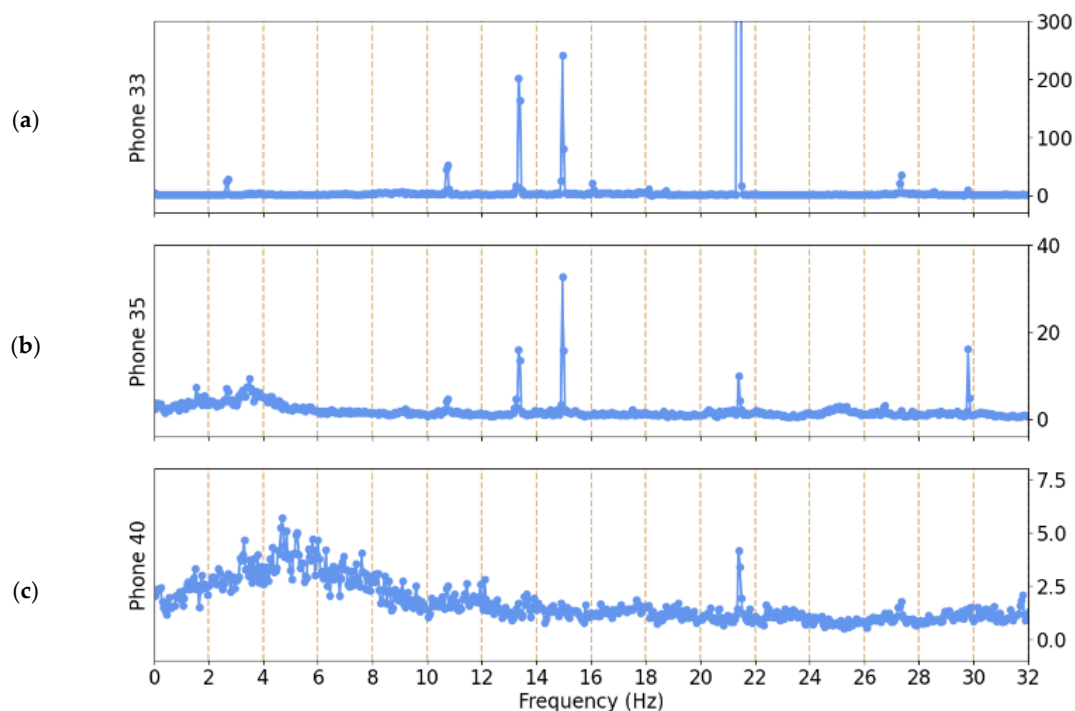


Figure 10. Low-frequency PDR calculated from the data collected during HFIR Cycle 487 during start-up operations and from smartphones 33, 35, and 40 shown in (a), (b), and (c), respectively.

To further highlight additional frequencies that were present during HFIR Cycle 487 start-up—including the frequencies identified for the dual-speed fan at 10.8 and 15.0 Hz—a spectrogram was computed and plotted between 5 and 35 Hz and is shown in Figure 11. The spectrogram was calculated using a Hann-tapered 10 s window with 50% overlap. No frequency-dependent gain correction was applied to the data and units were not converted to pascals since the focus was to highlight the signal-to-noise ratio and relative power in the different frequency bands. Power was calculated and displayed in decibels relative to the total mean value of the spectrogram.

The low-frequency noise mentioned and observed as a hump in the PDRs for Phone 40 is visible in the spectrogram (Figure 11c). Due to the phone's outdoor position on a hilltop, this noise is likely wind. In addition, the spectrogram for Phone 33 shows a 30 s dropout in data at approximately 95 and 98 min.

Acoustic power changes in the spectrograms specifically related to variations in HFIR power and fan speeds are observed most prominently in Phone 33, as observed in Figure 11a. The spectrogram shows an increase in broad-band power at approximately 50 min, which coincides with the reactor changing to 10% power. The broad-band power gradually increases until the reactor reaches 100% power at approximately 120 min. The 15.0 Hz

signal is active starting at approximately 115 min and is visible in Phone 33 and 35. The 10.8 Hz signal is present starting at approximately 95 min and becomes visibly stronger at 115 min in Phone 33. As in the work presented by Eaton et al., narrow-band horizontal striations corresponding to HFIR variable-speed fans are observed.

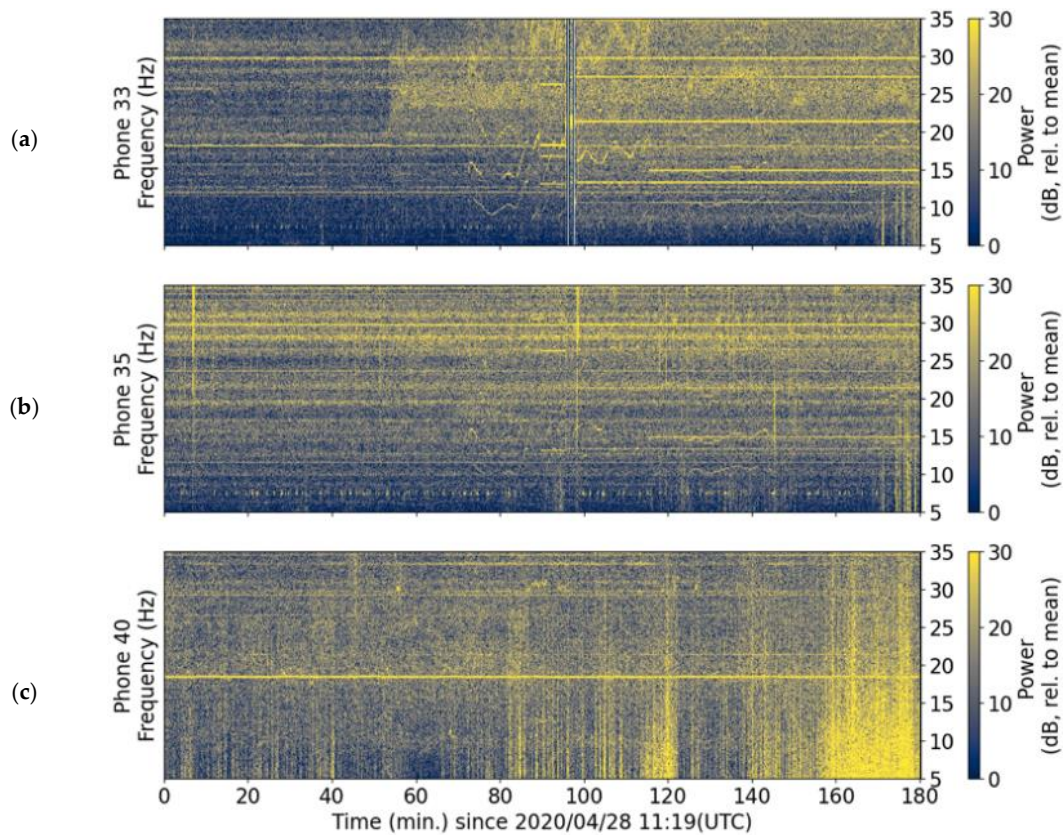


Figure 11. Spectrograms for HFIR Cycle 487 start-up for smartphones 33, 35, and 40 are shown in (a), (b), and (c), respectively.

4. Conclusions

An investigation of HFIR operating cycles that included start-up, shutdown, and steady-state power was conducted through acoustic analysis from data collected persistently on smartphones. This study, aimed at observations under nonideal conditions in the absence of meteorological data, used data collected from four operating cycles and smartphones that were 69, 101, and 914 m away from the HFIR cooling towers. Calculation of the PDR from acoustic pressure waves generated during HFIR steady-state on and HFIR off operations amplifies dominant acoustic frequencies related to reactor power. Implementing the method of isolating these dominant acoustic frequencies, followed by summing them and calculating the RMS, reveals acoustic behavior that more closely matches the behavior of reactor power, especially in sensors farther from the emission source.

Results were consistent with papers published under the MINOS venture, where the 21.4 Hz fundamental frequency and related harmonics are associated with dual-speed fan operations. This paper supports those claims by showing acoustic signals that vary in agreement with logs noting fan changes. Additional observed tonal frequencies were related to the blade-passing and motor frequencies of the variable-speed fans and the maximum rotational speed of the HFIR cooling tower fans. This research provides insight into using persistent acoustic monitoring as a diagnostic method useful in circumstances where on-equipment monitoring is not feasible. Enhancements to improve this work may include calculations of expected power levels in relation to distances from the cooling tower, as well as comparisons of smartphone acoustic measurements with more traditional infrasound sensors.

Supplementary Materials: The following supporting information can be downloaded at: <https://www.mdpi.com/article/10.3390/acoustics5020025/s1>, Figure S1: Acoustic RMS power for HFIR Cycle 488-B start-up. Figure S2: Acoustic RMS power for HFIR Cycle 489 start-up. Figure S3: Acoustic RMS power for HFIR Cycle 490 start-up.

Author Contributions: Writing—original draft preparation, investigation: E.S.C. and S.K.T.; conceptualization, methodology: E.S.C., S.K.T., M.A.G. and D.L.C.; data curation: S.K.T., M.A.G., R.D.H. and C.D.Y.; resources: M.A.G. and D.L.C.; writing—review and editing: E.S.C., S.K.T., D.L.C., M.A.G., R.D.H. and C.D.Y.; project administration: D.L.C.; funding acquisition: D.L.C. All authors have read and agreed to the published version of the manuscript.

Funding: This research was supported by the U.S. Department of Energy (DOE) National Nuclear Security Administration (NNSA) Office of Proliferation Detection. Idaho National Laboratory is managed by the Department of Energy under contract number DE-AC07-05ID14517. M. Garces and K. Takazawa were also supported by the U.S. DOE NNSA under Award Numbers DE-NA0003920 (MTV) and DE-NA0003921 (ETI).

Data Availability Statement: Restrictions apply to the availability of these data. Data were generated at Oak Ridge National Laboratory and are available with the permission of the U.S. Department of Energy, National Nuclear Security Administration, Office of Defense Nuclear Nonproliferation Research and Development. To request data access, contact Jared Johnson (johnsonja@ornl.gov).

Acknowledgments: We are grateful to A. Christe, B. Williams, T. Yoshiyama, K. Asmar, and J. Tobin for their contributions to the MINOS project and the development of fundamental methods. We would also like to thank S. M. Watson and T. Holschuh for their participation in the project and L. Ocampo Giraldo and G. E. Holt for their reviews of the manuscript.

Conflicts of Interest: The authors declare no conflict of interest. The funders had no role in the design of the study; in the collection, analyses, or interpretation of data; in the writing of the manuscript; or in the decision to publish the results.

References

1. Stromkov, A.; Didenkulov, I.N.; Karlik, Y.S.; Petropavlovsk-Kamchatski, P. Acoustic detection of tsunamis in the open sea. In Proceedings of the Petropavlovsk-Kamchatsky Tsunami Workshop, Petropavlovsk-Kamchatsky, Russia, 10–15 September 2002; pp. 55–62.
2. Bedard, A.J. Detection of avalanches using atmospheric infrasound. In Proceedings of the 57th Annual Meeting of the Western Snow Conference, Fort Collins, CO, USA, 18 April 1989; pp. 52–59.
3. Bedard, J.A.J.; Bloemker, R. Detection of space debris and meteor impacts using atmospheric infrasound. *Small Spacecr. Space Environ. Instrum. Technol.* **1997**, *3116*, 177–192. [[CrossRef](#)]
4. Bedard, A.J.; Georges, T.M. Atmospheric Infrasound. *Phys. Today* **2000**, *53*, 32–37. [[CrossRef](#)]
5. Le Pichon, A.; Herry, P.; Mialle, P.; Vergoz, J.; Brachet, N.; Garcés, M.; Drob, D.; Ceranna, L. Infrasound associated with 2004–2005 large Sumatra earthquakes and tsunami. *Geophys. Res. Lett.* **2005**, *32*, e2005GL023893. [[CrossRef](#)]
6. Garces, M.; Caron, P.; Hetzer, C.; Le Pichon, A.; Bass, H.; Drob, D.; Bhattacharyya, J. Deep infrasound radiated by the Sumatra earthquake and tsunami. *Eos. Trans. Am. Geophys. Union* **2005**, *86*, 317. [[CrossRef](#)]
7. Allstadt, K.E.; Matoza, R.S.; Lockhart, A.B.; Moran, S.C.; Caplan-Auerbach, J.; Haney, M.M.; Thelen, W.A.; Malone, S.D. Seismic and acoustic signatures of surficial mass movements at volcanoes. *J. Volcanol. Geotherm. Res.* **2018**, *364*, 76–106. [[CrossRef](#)]
8. De Angelis, S.; Diaz-Moreno, A.; Zuccarello, L. Recent Developments and Applications of Acoustic Infrasound to Monitor Volcanic Emissions. *Remote. Sens.* **2019**, *11*, 1302. [[CrossRef](#)]
9. Bedard, A.J. Low-Frequency Atmospheric Acoustic Energy Associated with Vortices Produced by Thunderstorms. *Mon. Weather. Rev.* **2005**, *133*, 241–263. [[CrossRef](#)]
10. McKisic, J.M. *Infrasound and the Infrasonic Monitoring of Atmospheric Nuclear Explosions: A Literature Review*; U.S. Department of Energy Office of Non-Proliferation and National Security: Washington, DC, USA, 1997. Available online: <https://apps.dtic.mil/sti/pdfs/ADA339249.pdf> (accessed on 19 September 2022).
11. CTBTO Preparatory Commission, n.d., “Infrasound Monitoring,” Webpage [Online]. Available online: <https://www.ctbto.org/verification-regime/monitoring-technologies-how-they-work/infrasound-monitoring/> (accessed on 19 September 2022).
12. Bowman, D.C.; Krishnamoorthy, S. Infrasound From a Buried Chemical Explosion Recorded on a Balloon in the Lower Stratosphere. *Geophys. Res. Lett.* **2021**, *48*, e2021GL094861. [[CrossRef](#)]
13. Che, I.-Y.; Park, J.; Kim, I.; Kim, T.S.; Lee, H.-I. Infrasound signals from the underground nuclear explosions of North Korea. *Geophys. J. Int.* **2014**, *198*, 495–503. [[CrossRef](#)]
14. Blom, P.; Marcillo, O.; Arrowsmith, S. Analysis and modeling of infrasound from a four-stage rocket launch. *J. Acoust. Soc. Am.* **2016**, *139*, 3134–3138. [[CrossRef](#)]

15. Ishihara, Y.; Hiramatsu, Y.; Yamamoto, M.-Y.; Fujita, K. Infrasound/seismic observation of the Hayabusa reentry: Observations and preliminary results. *Earth Planets Space* **2012**, *64*, 655–660. [CrossRef]
16. Evers, L.G.; Assink, J.; Smets, P. Infrasound from the 2009 and 2017 DPRK rocket launches. *Geophys. J. Int.* **2018**, *213*, 1785–1791. [CrossRef]
17. Balachandran, N.K.; Donn, W.L. Characteristics of Infrasonic Signals from Rockets. *Geophys. J. R. Astron. Soc.* **1971**, *26*, 135–148. [CrossRef]
18. Donn, W.L.; Balachandran, N.K.; Kaschak, G. Atmospheric infrasound radiated by bridges. *J. Acoust. Soc. Am.* **1974**, *56*, 1367–1370. [CrossRef]
19. Whitlow, R.D.; Haskins, R.; McComas, S.L.; Crane, C.K.; Howard, I.L.; McKenna, M.H. Remote Bridge Monitoring Using Infrasound. *J. Bridg. Eng.* **2019**, *24*, 1–11. Available online: <https://ascelibrary.org/doi/10.1061/%28ASCE%29BE.1943-5592.0001375%28ASCE%29BE.1943-5592.0001375> (accessed on 19 September 2022). [CrossRef]
20. Hubbard, H.H.; Shepherd, K.P. Aeroacoustics of large wind turbines. *J. Acoust. Soc. Am.* **1991**, *89*, 2495–2508. [CrossRef]
21. Bilski, B. Exposure to infrasonic noise in agriculture. *Ann. Agric. Environ. Med.* **2017**, *24*, 86–89. [CrossRef]
22. Nowacki, G.; Mitraszewska, I.; Kamiński, T.; Wierzejski, A. Research of infrasound noise in heavy goods vehicles and busses. In Proceedings of the 8th International Conference on Reliability and Statistics in Transportation and Communication, Riga, Latvia, 15–18 October 2008; pp. 209–215. Available online: <https://citeseerx.ist.psu.edu/viewdoc/download?doi=10.1.1.520.6326&rep=rep1&type=pdf> (accessed on 19 September 2022).
23. Kudźma, Z.; Stosiak, M. Reduction of infrasounds in machines with hydrostatic drive. *Acta Bioeng. Biomech.* **2013**, *15*, 51–64. Available online: <https://actabio.pwr.edu.pl/Vol15No2/6.pdf> (accessed on 19 September 2022). [PubMed]
24. Liszka, L. Long-distance propagation of infrasound from artificial sources. *J. Acoust. Soc. Am.* **1974**, *56*, 1383–1388. [CrossRef]
25. Le Pichon, A.; Blanc, E.; Hauchecorne, A. *Infrasound Monitoring for Atmospheric Studies: Challenges in Middle Atmosphere Dynamics and Societal Benefits*; Springer: Cham, Switzerland, 2019.
26. Flynn, G.S.; Parikh, N.; Egid, K.A.; Casleton, E. *Predicting Power Levels of a Nuclear Reactor by Combining Multiple Modalities*; LA-UR-19-26714; Los Alamos National Laboratory: Los Alamos, NM, USA, 2019.
27. Chichester, D.L.; Garcés, M.A.; Watson, S.M.; Johnson, J.T.; Christe, A.J.; Cárdenas, E.S.; Asmar, K.A. Use of infrasound to monitor nuclear facilities. In Proceedings of the 59th Annual Meeting of the Institute of Nuclear Material Management (INMM 2018), Baltimore, MD, USA, 22–26 July 2018; Institute of Nuclear Materials Management, Curran Associates, Inc.: Red Hook, NY, USA; Volume 3, pp. 1912–1921.
28. Chichester, D.L.; Garcés, M.A.; Watson, S.M.; Cárdenas, E.S.; Maceira, M.; Christe, A.J.; Holschuh, T.V. Initial assessment of infrasound signatures tied to nuclear facility operations. In Proceedings of the 60th Annual Meeting of the Institute of Nuclear Material Management (INMM 2019), Palm Desert, CA, USA, 14–18 July 2019; Volume 2, pp. 765–774.
29. Cárdenas, E.S.; Garcés, M.A.; Krebs, J.F.; Watson, S.M.; Johnson, J.T.; Hix, J.D.; Chichester, D.L. Persistent Acoustic Sensing for Monitoring a Reactor Facility, in Institute of Nuclear Materials Management (INMM 2021), Virtual [Online]. 2021. Available online: <https://resources.inmm.org/sites/default/files/2021-09/a296.pdf> (accessed on 15 December 2022).
30. Marcillo, O.E.; Maceira, M.; Chai, C.; Gammans, C.; Hunley, R.; Young, C. The Local Seismoacoustic Wavefield of a Research Nuclear Reactor and Its Response to Reactor Power Level. *Seism. Res. Lett.* **2020**, *92*, 378–387. [CrossRef]
31. Chai, C.; Ramirez, C.; Maceira, M.; Marcillo, O. Monitoring Operational States of a Nuclear Reactor Using Seismoacoustic Signatures and Machine Learning. *Seism. Res. Lett.* **2022**, *93*, 1660–1672. [CrossRef]
32. Chai, C.P.; Maceira, M.; Marcillo, O.E. Oak Ridge National Laboratory Seismo-Acoustic Characteristics of HFIR Cooling Tower Fans and Pumps, ORNL/TM-2021/2308, Oak Ridge National Laboratory, Oak Ridge, TN, USA [Online]. 2021. Available online: <https://info.ornl.gov/sites/publications/Files/Pub169700.pdf> (accessed on 19 September 2022).
33. Eaton, S.W.; Cárdenas, E.S.; Hix, J.D.; Johnson, J.T.; Watson, S.M.; Chichester, D.L.; Garcés, M.A.; Magaña-Zook, S.A.; Maceira, M.; Marcillo, O.E.; et al. An algorithmic approach to predicting mechanical draft cooling tower fan speeds from infrasound signals. *Appl. Acoust.* **2022**, *199*, 10915. [CrossRef]
34. Oak Ridge National Laboratory. High Flux Isotope Reactor (HFIR) User Guide: A Guide to In-Vessel Irradiations and Experiments, 2015, Oak Ridge National Laboratory, Oak Ridge, TN, USA [Online]. 2015. Available online: <https://neutrons.ornl.gov/sites/default/files/High%20Flux%20Isotope%20Reactor%20User%20Guide%202.0.pdf> (accessed on 19 September 2022).
35. Rao, N.S.V.; Greulich, C.; Sen, S.; Dayman, K.J.; Hite, J.; Ray, W.; Hale, R.; Nicholson, A.D.; Johnson, J.; Hunley, R.D.; et al. Reactor power level estimation by fusing multi-modal sensor measurements. In Proceedings of the 2020 IEEE 23rd International Conference on Information Fusion (Fusion 2020), Rustenburg, South Africa, 6–9 July 2020; pp. 857–864. Available online: <https://ieeexplore.ieee.org/stamp/stamp.jsp?tp=&arnumber=9190219> (accessed on 19 September 2022).
36. Tsunekawa, S.; Kajikawa, Y.; Nohara, S.; Ariizumi, M.; Okada, A. Study on the perceptible level for infrasound. *J. Sound Vib.* **1987**, *112*, 15–22. [CrossRef]
37. Broner, N. A Simple Criterion for Low Frequency Noise Emission Assessment. *J. Low Freq. Noise Vib. Act. Control* **2010**, *29*, 1–13. [CrossRef]
38. Garcés, M.A.; Bowman, D.; Zeiler, C.; Christe, A.; Yoshiyama, T.; Williams, B.; Colet, M.; Takazawa, S.; Popenhagen, S. Skyfall: Signal Fusion from a Smartphone Falling from the Stratosphere. *Signals* **2022**, *3*, 209–234. [CrossRef]

39. Welch, P.D. The use of fast Fourier transform for the estimation of power spectra: A method based on time averaging over short, modified periodograms. *IEEE Trans. Audio Electroacoust.* **1967**, *15*, 70–73. Available online: <https://ieeexplore.ieee.org/stamp/stamp.jsp?tp=&arnumber=1161901> (accessed on 19 September 2022). [[CrossRef](#)]
40. Salawu, O.S. Detection of structural damage through changes in frequency: A review. *Eng. Struct.* **1997**, *19*, 718–723. [[CrossRef](#)]

Disclaimer/Publisher’s Note: The statements, opinions and data contained in all publications are solely those of the individual author(s) and contributor(s) and not of MDPI and/or the editor(s). MDPI and/or the editor(s) disclaim responsibility for any injury to people or property resulting from any ideas, methods, instructions or products referred to in the content.